Supplemental material for "Symmetry breaking and spectral structure of the interacting Hatano-Nelson model"

Song-Bo Zhang,[1] M. Michael Denner,[1] Tomáš Bzdušek,[2,1] Michael A. Sentef,[3] and Titus Neupert[1]

[1] *Department of Physics, University of Zürich, Winterthurerstrasse 190, 8057, Zürich, Switzerland*
[2] *Condensed Matter Theory Group, Paul Scherrer Institute, 5232 Villigen PSI, Switzerland*
[3] *Max Planck Institute for the Structure and Dynamics of Matter, Luruper Chaussee 149, 22761 Hamburg, Germany*

(Dated: August 25, 2022)

In this Supplemental Material, we present the analysis of the system symmetries (Sec. I), Pauli exclusion principle (Sec. II), dimensions of the many-body spectrum (Sec. III), more discussions of critical interaction strength (Sec. IV), density-density correlation (Sec. V), free energy and persistent current (Sec. VI), spectral winding numbers and charge-density profiles (Sec. VII), other complementary half-filled cases (Sec. VIII), and the non-Hermitian SSH-type model (Sec. IX).

I. $\mathcal{PT}$ AND PARTICLE-HOLE SYMMETRIES

For general twisted periodic boundary conditions (PBC) characterized by a twist boundary angle ϕ, the Hamiltonian reads

$$\hat{H}=\sum_{\ell=1}^{L-1}[(t+\gamma)\hat{c}_{\ell}^{\dagger}\hat{c}_{\ell+1}+(t-\gamma)\hat{c}_{\ell+1}^{\dagger}\hat{c}_{\ell}+U\hat{n}_{\ell}\hat{n}_{\ell+1}]+e^{i\phi}(t+\gamma)\hat{c}_{L}^{\dagger}\hat{c}_{1}+e^{-i\phi}(t-\gamma)\hat{c}_{1}^{\dagger}\hat{c}_{L}+U\hat{n}_{L}\hat{n}_{1}, \tag{1}$$

Particularly, $\phi=0$ and π correspond to PBC and anti-PBC, respectively. We define the $\mathcal{PT}$ symmetry operation as

$$\mathcal{PT}\hat{c}_{\ell}(\mathcal{PT})^{-1}=\hat{c}_{L+1-\ell},\quad \mathcal{PT}i(\mathcal{PT})^{-1}=-i. \tag{2}$$

Acting with $\mathcal{PT}$ on $\hat{H}$, we find

$$\begin{aligned}
&\mathcal{PT}\hat{H}(\mathcal{PT})^{-1}\\
=&\mathcal{PT}\Big\{\sum_{\ell=1}^{L-1}[(t+\gamma)\hat{c}_{\ell}^{\dagger}\hat{c}_{\ell+1}+(t-\gamma)\hat{c}_{\ell+1}^{\dagger}\hat{c}_{\ell}+U\hat{n}_{\ell}\hat{n}_{\ell+1}]+e^{i\phi}(t+\gamma)\hat{c}_{L}^{\dagger}\hat{c}_{1}+e^{-i\phi}(t-\gamma)\hat{c}_{1}^{\dagger}\hat{c}_{L}+U\hat{n}_{L}\hat{n}_{1}\Big\}(\mathcal{PT})^{-1}\\
=&\sum_{\ell=1}^{L-1}[(t+\gamma)\hat{c}_{L+1-\ell}^{\dagger}\hat{c}_{L-\ell}+(t-\gamma)\hat{c}_{L-\ell}^{\dagger}\hat{c}_{L+1-\ell}+U\hat{n}_{L+1-\ell}\hat{n}_{L-\ell}]+e^{-i\phi}(t+\gamma)\hat{c}_{1}^{\dagger}\hat{c}_{L}+e^{i\phi}(t-\gamma)\hat{c}_{L}^{\dagger}\hat{c}_{1}+U\hat{n}_{1}\hat{n}_{L}\\
=&\sum_{\jmath=1}^{L-1}[(t+\gamma)\hat{c}_{\jmath+1}^{\dagger}\hat{c}_{\jmath}+(t-\gamma)\hat{c}_{\jmath}^{\dagger}\hat{c}_{\jmath+1}+U\hat{n}_{\jmath+1}\hat{n}_{\jmath}]+[e^{i\phi}(t+\gamma)\hat{c}_{L}^{\dagger}\hat{c}_{1}+e^{-i\phi}(t-\gamma)\hat{c}_{1}^{\dagger}\hat{c}_{L}]^{\dagger}+U\hat{n}_{1}\hat{n}_{L}.
\end{aligned} \tag{3}$$

In the last line, we have replaced $\jmath=L-\ell$. For PBC and anti-PBC, it follows that

$$\mathcal{PT}\hat{H}(\mathcal{PT})^{-1}=\hat{H}^{\dagger}. \tag{4}$$

This relation indicates that the eigenenergies of $\hat{H}$ must either be real or come in complex-conjugate pairs.

To see the particle-hole symmetry explicitly, we divide the lattices into two sublattices A and B of even and odd sites. We perform the transformation $\hat{c}_{\ell}^{\dagger}\to\hat{c}_{\ell}$ and $\hat{c}_{\ell}\to\hat{c}_{\ell}^{\dagger}$ on sublattice A while $\hat{c}_{\ell}^{\dagger}\to-\hat{c}_{\ell}$ and $\hat{c}_{\ell}\to-\hat{c}_{\ell}^{\dagger}$ on sublattice B. Accordingly, the transformation for the occupation number operators reads $\hat{n}_{\ell}\to1-\hat{n}_{\ell}$. Then, it is clear to see that the transformed Hamiltonian takes the same form up to a constant energy shift.

II. PAULI EXCLUSION PRINCIPLE

In this work, we consider the interacting Hatano-Nelson model which can be written in the basis of conventional fermionic operators $\hat{c}_{\ell}^{\dagger}$ and $\hat{c}_{\ell}$ as

$$\hat{H}=\sum_{\ell=1}^{L}[(t+\gamma)\hat{c}_{\ell}^{\dagger}\hat{c}_{\ell+1}+(t-\gamma)\hat{c}_{\ell+1}^{\dagger}\hat{c}_{\ell}+U\hat{n}_{\ell}\hat{n}_{\ell+1}]. \tag{5}$$

The fermionic operators $\hat{c}_\ell^\dagger$ and $\hat{c}_\ell$ follow the anticommutation relations

$$\{\hat{c}_\ell^\dagger, \hat{c}_\jmath\} = \delta_{\ell,\jmath}, \quad \{\hat{c}_\ell, \hat{c}_\jmath\} = 0. \tag{6}$$

With these relations, we find that the number operator $\hat{n}_\jmath \equiv \hat{c}_\jmath^\dagger \hat{c}_\jmath$ at site $\jmath$ follows the relation

$$\hat{n}_\jmath^2 = \hat{c}_\jmath^\dagger \hat{c}_\jmath \hat{c}_\jmath^\dagger \hat{c}_\jmath = \hat{c}_\jmath^\dagger \left(1 - \hat{c}_\jmath^\dagger \hat{c}_\jmath\right) \hat{c}_\jmath = \hat{c}_\jmath^\dagger \hat{c}_\jmath = \hat{n}_\jmath, \tag{7}$$

which gives $\hat{n}_\jmath = 0$ or 1. This means that an arbitrary site $\jmath$ is at most occupied by one electron, which is the Pauli exclusion principle considered in this work.

The singe-particle eigenstates also follow the Pauli exclusion principle. To illustrate this, we rewrite the single-particle Hamiltonian (with $U = 0$) as

$$\hat{H} = \sum_n E_n |R_n\rangle\langle L_n|, \tag{8}$$

where $|L_n\rangle$ and $|R_n\rangle$ are the left and right eigenstates of $\hat{H}$, satisfying $\hat{H}|R_n\rangle = E_n|R_n\rangle$ and $\hat{H}^\dagger|L_n\rangle = E_n^*|R_n\rangle$, respectively. The left and right eigenstates have the biorthogonal relations $\langle L_m|R_n\rangle = \delta_{m,n}$. If we define $d_{n,R}^\dagger$ ($d_{n,L}^\dagger$) as the creation operator related to the eigenstate $|R_n\rangle$ ($|L_n\rangle$),

$$d_{n,R}^\dagger = \sum_\ell \langle \ell|R_n\rangle \hat{c}_\ell^\dagger, \tag{9}$$

then we find that these operators have the following modified anticommutation relations

$$\begin{aligned} &\{d_{m,R}^\dagger, d_{n,L}\} = \delta_{m,n}, \\ &\{d_{m,R}^\dagger, d_{n,R}^\dagger\} = 0, \\ &\{d_{m,R}^\dagger, d_{n,R}\} = \langle R_n|R_m\rangle. \end{aligned} \tag{10}$$

Note that for non-Hermitian system, not all the eigenstates $|R_m\rangle$ are orthogonal, i.e., $\langle R_n|R_m\rangle$ could be finite even for $m \neq n$. Using the modified anticommutation relations in Eq. (10), we find that the number operator $\hat{\aleph}_m \equiv d_{m,R}^\dagger d_{m,R}$ for the eigenstate $|R_m\rangle$ follows

$$\hat{\aleph}_m^2 = d_{m,R}^\dagger \left(\langle R_m|R_m\rangle - d_{m,R}^\dagger d_{m,R}\right) d_{m,R} = \langle R_m|R_m\rangle \hat{\aleph}_m. \tag{11}$$

Thus, $\hat{\aleph}_m$ can only have the eigenvalues 0 and $\langle R_m|R_m\rangle$, where the latter can be different from 1 (in particular larger). Similar results can be obtained for the left eigenstates. These results show that the eigenstates also obey the Pauli exclusion principle, i.e., a fermionic state can be occupied at most by one particle simultaneously.

III. DIMENSION OF THE MANY-BODY SPECTRUM

The extent of the spectrum at $U = 0$ on the real and imaginary axes can be written as

$$\Xi_{\rm R} \approx t\alpha_{\{N,L\}} \text{ and } \Xi_{\rm I} \approx \gamma\alpha_{\{N,L\}}, \tag{12}$$

where κ are integers, $n_{\rm cl} \equiv \min(N, L-N)$ and

$$\alpha_{\{N,L\}} = 2 \sum_{|\kappa| \leqslant n_{\rm cl}/2} \cos(2\pi\kappa/L). \tag{13}$$

For $n_{\rm cl} \gg 1$, we transform the summation in Eq. (13) to an integral and obtain

$$\alpha_{\{N,L\}} = \frac{2L}{\pi} \sin\left(\frac{n_{\rm cl}\pi}{L}\right). \tag{14}$$

At half-filling, $n_{\rm cl} = L/2$. Thus, $\alpha_{\{N,L\}}$ simplifies to

$$\alpha_{\{N,L\}} = \frac{2L}{\pi}. \tag{15}$$

IV. CRITICAL INTERACTION STRENGTH IN THE THERMODYNAMIC LIMIT

The dependence of U_c on L follows a power-law scaling, as shown in Fig. S1(a). The circle dots are numerical results obtained by exact diagonalization while the curves are the fitting with the power-law relation, Eq. (2) in the main text. The extrapolated $U_c = U_{\rm TD}$ in the TDL is shown by the red line in Fig. 1(c) of the main text. The fitting parameters α and β depend explicitly on γ, as shown in Fig. S1(b).

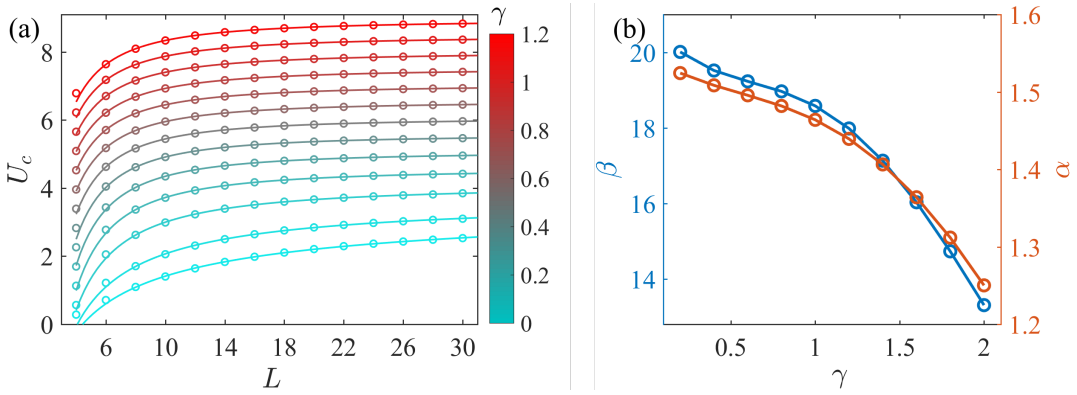

Fig. S1. (a) Critical interaction strength U_c as a function of L for different nonreciprocity γ. The color changes from cyan to red when γ increases from 0 to $1.2t$. The circle dots are exact diagonalization results and the curves are the fitting with the power-law relation, Eq. (2), in the main text. (b) Extrapolated index α (right orange) and decaying strength β (left blue) as functions of γ.

V. DENSITY-DENSITY CORRELATION FUNCTION

To characterize the phase diagram, we compute the density-density correlation function by [1]

$$\begin{aligned}\mathcal{C}_\ell &= \langle(\hat{n}_0 - 1/2)(\hat{n}_\ell - 1/2)\rangle \\ &= \frac{\sum_j \langle j|(\hat{n}_0 - 1/2)(\hat{n}_\ell - 1/2)e^{-\beta E_j}|j\rangle}{\mathcal{Z}},\end{aligned} \tag{16}$$

where $|j\rangle$ are the right eigenstates of the many-body Hamiltonian with eigenvalues E_j, $\mathcal{Z}$ is the partition function given by Eq. (18). For concreteness, we consider the long-range correlation function with $\ell = L/2$ and at low temperatures $1/\beta = k_B T \ll t$. In the low-temperature limit $\beta \to \infty$, Eq. (16) describes the density-density correlation of the ground state. The correlation function as a function of interaction strength U for increasing L is shown in Fig. S2. At $U = 0$, we find $\mathcal{C}_{L/2} = 0$. When increasing U, $|\mathcal{C}_{L/2}|$ increases slowly in the small U regime but rapidly around

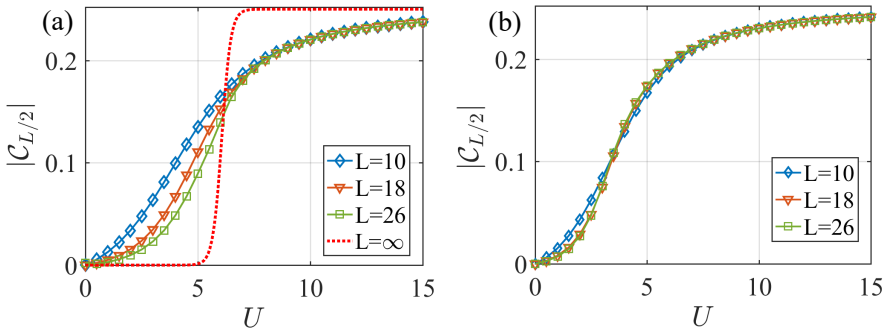

Fig. S2. (a) Density-density correlation function as a function of U for different L. The red dotted curve sketches the result in the TDL. Other parameters are $\gamma = 0.6t$ and $k_B T = 0.1t$. (b) is the same as (a) but for the Hermitian limit $\gamma = 0$.

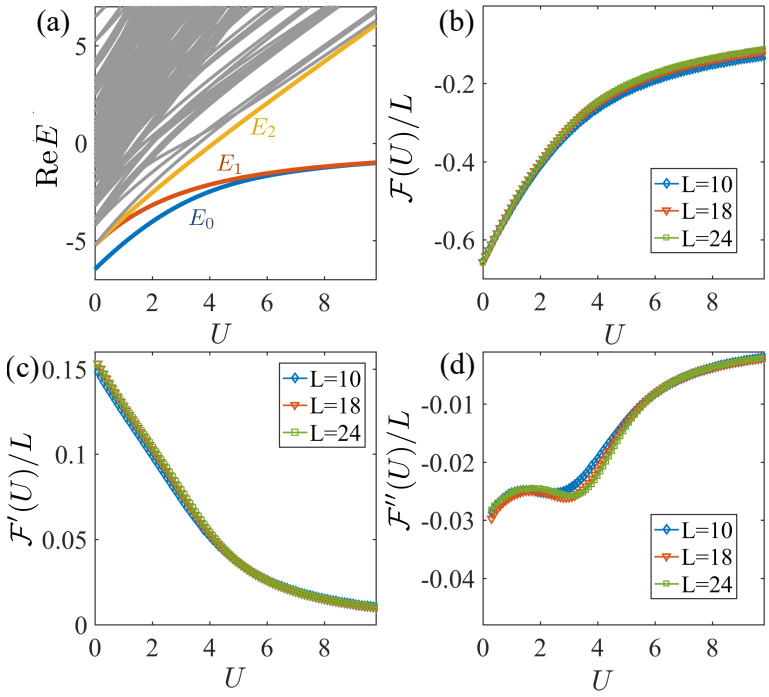

Fig. S3. (a) Real part of the low-Re(E) spectrum as a function of U. We take $L = 10$ for illustration. (b) Free energy $\mathcal{F}(U)$, its first (b) $\mathcal{F}'(U)$ and second (c) derivative $\mathcal{F}''(U)$ as functions of U. In contrast to the case with finite $\gamma \neq 0$, $\mathcal{F}$ and its derivatives change smoothly when increasing U. $\gamma = 0$ and other parameters are the same as Fig. 3 in the main text.

$U = U_c$. In the large U regime, $|\mathcal{C}_{L/2}|$ saturates slowly to a universal value 0.25. For larger systems, these features are more pronounced. In the TDL, we can expect $|\mathcal{C}_{L/2}|$ to suddenly jump from zero to the universal value 0.25 at the transition, as sketched by the red dotted curve in Fig. S2(a). A similar behavior of $|\mathcal{C}_{L/2}|$ happens for $\gamma = 0$ but with the rapid increment around a smaller U, as shown in Fig. S2(b). Finally, we note that for odd $L/2$, we have always $\mathcal{C}_{L/2} \geq 0$, while for even $L/2$, we have always $\mathcal{C}_{L/2} \leq 0$. This reflects the fact that the ground state of the system is likely to have staggered charge-density distribution, namely, different charge densities at odd and even lattice sites.

VI. FREE ENERGY AND PERSISTENT CURRENT

The free energy $\mathcal{F}$ of the interacting system at temperature T is given by

$$\mathcal{F} = -\frac{1}{\beta}\log\mathcal{Z}, \tag{17}$$

where $\beta = 1/k_{\rm B}T$ with $k_{\rm B}$ being the Boltzmann constant, and $\mathcal{Z}$ is the partition function

$$\mathcal{Z} = \sum_j e^{-\beta E_j}. \tag{18}$$

The sum in Eq. (18) runs over all eigenenergies. In the Hermitian limit $\gamma = 0$, all eigenenergies change smoothly with increasing U [Fig. S3(a)]. Consequently, $\mathcal{F}$ and its derivative also change smoothly, as shown in Figs. S3(b–d).

The application of a magnetic flux ϕ thread through the ring changes the eigenenergies and hence $\mathcal{F}$ periodically. The persistent current along the ring can be found as the derivative of $\mathcal{F}$ with respect to ϕ [2], i.e.,

$$I_{\rm p} = -\frac{e}{\hbar}\frac{\partial\mathcal{F}}{\partial\phi}, \tag{19}$$

where e is the elementary charge and $\hbar$ the reduced Planck constant.

At zero temperature, the free energy is equal to the ground-state energy, i.e., $\mathcal{F} = E_0$. In the absence of interactions, the ground-state energy can be found as

$$E_0(\phi) = -2 \sum_{|\kappa| \leqslant L/4} \Big[t \cos\Big(\frac{2\pi\kappa}{L} + \frac{\phi}{L}\Big) + i\gamma \sin\Big(\frac{2\pi\kappa}{L} + \frac{\phi}{L}\Big)\Big], \tag{20}$$

where κ are integers. For $L \gg 1$, we approximate the summation in Eq. (20) as an integral and obtain

$$\begin{aligned} E_0(\phi) &= -\frac{L}{\pi} \int_{-\pi/2}^{\pi/2} dx \Big[t\cos(x)\cos\Big(\frac{\phi}{L}\Big) - t\sin(x)\sin\Big(\frac{\phi}{L}\Big) + i\gamma\sin(x)\cos\Big(\frac{\phi}{L}\Big) + i\gamma\cos(x)\sin\Big(\frac{\phi}{L}\Big)\Big] \\ &= -\frac{2L}{\pi}\Big[t\cos\Big(\frac{\phi}{L}\Big) + i\gamma\sin\Big(\frac{\phi}{L}\Big)\Big]. \end{aligned} \tag{21}$$

Plugging $\mathcal{F} = E_0$ into Eq. (19), we find

$$I_{\rm p} = \frac{2e}{\hbar\pi}\Big[-t\sin\Big(\frac{\phi}{L}\Big) + i\gamma\cos\Big(\frac{\phi}{L}\Big)\Big]. \tag{22}$$

At zero flux $\phi = 0$, the persistent current is given by

$$I_{\rm p} = i\frac{2e}{\hbar}\frac{\gamma}{\pi}. \tag{23}$$

VII. NONTRIVIAL WINDING NUMBERS AND CHARGE DENSITY PROFILES OF THE MANY-BODY EIGENSTATES

At $U = 0$, the flow of the eigenenergies as varying the twist boundary angle ϕ in a period $[0, 2\pi)$, and charge-density profiles of all many-body sates are shown in Fig. S4. In the strong interaction regime, the flow of the eigenenergies and charge-density profiles of the many-body eigenstates associated with the spectral clusters (i.e., with the energies close to the respective cluster energy centers) are shown in Fig. S5. Clearly, all the eigenenergies wind around the corresponding energy centers when ϕ increases from 0 to 2π. Correspondingly, the charge densities of the many-body eigenstates, which are evenly distributed in the system under PBC, tend to localize to an open boundary. We note that the winding numbers defined by Eq. (3) in the main text are applicable to finite-size systems. Due to the finite-size effect, all eigenenergies are away from the energy centers of clusters, provided that U is finite. Thus, the clusters have well-defined point gaps in finite-size systems. In the $L \to \infty$ limit but with fixed N, each clusters has at least one continuous orbit surrounding their energy centers. Nontrivial topological invariants can be defined as the winding numbers along these orbits.

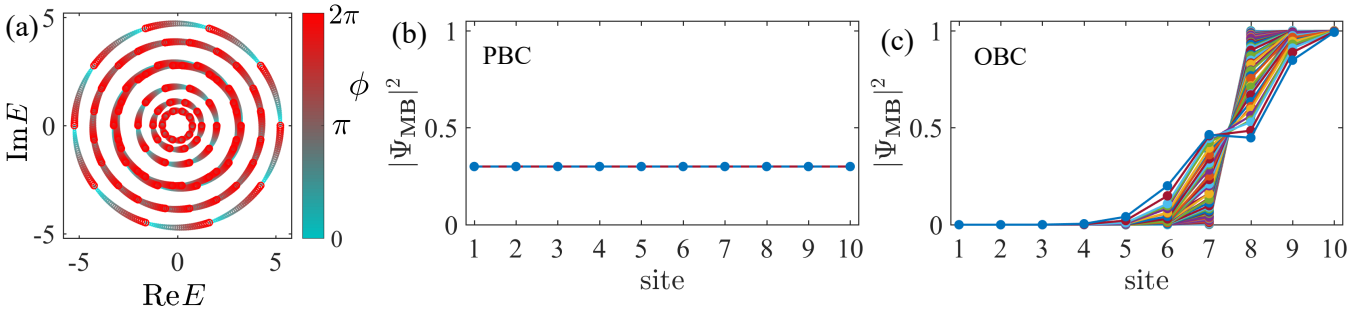

Fig. S4. (a) Movement of the eigenenergies at $U = 0$ as the twist boundary angle ϕ increases from 0 (cyan) to 2π (red). All eigenenergies wind around $E = 0$ in one direction. The spectral winding number for the spectrum is found as $\nu = 12$. (b) Charge density profiles of all many-body states under PBC. (c) the same as (b) but for OBC. We consider $L = 10$, $N = 3$, $U = 20t$ and a relatively large $\gamma = 0.9t$ for better illustration.

Figure S6 plots the clusters for fixed N and increasing L. We see that as L grows, the eigenenergies fill the clusters more densely. In the TDL, the clusters form continuous areas and orbits in the complex-energy plane. Thus, we can always find a continuous orbit of eigenenergies that surround the energy center of any cluster. A nonzero topological

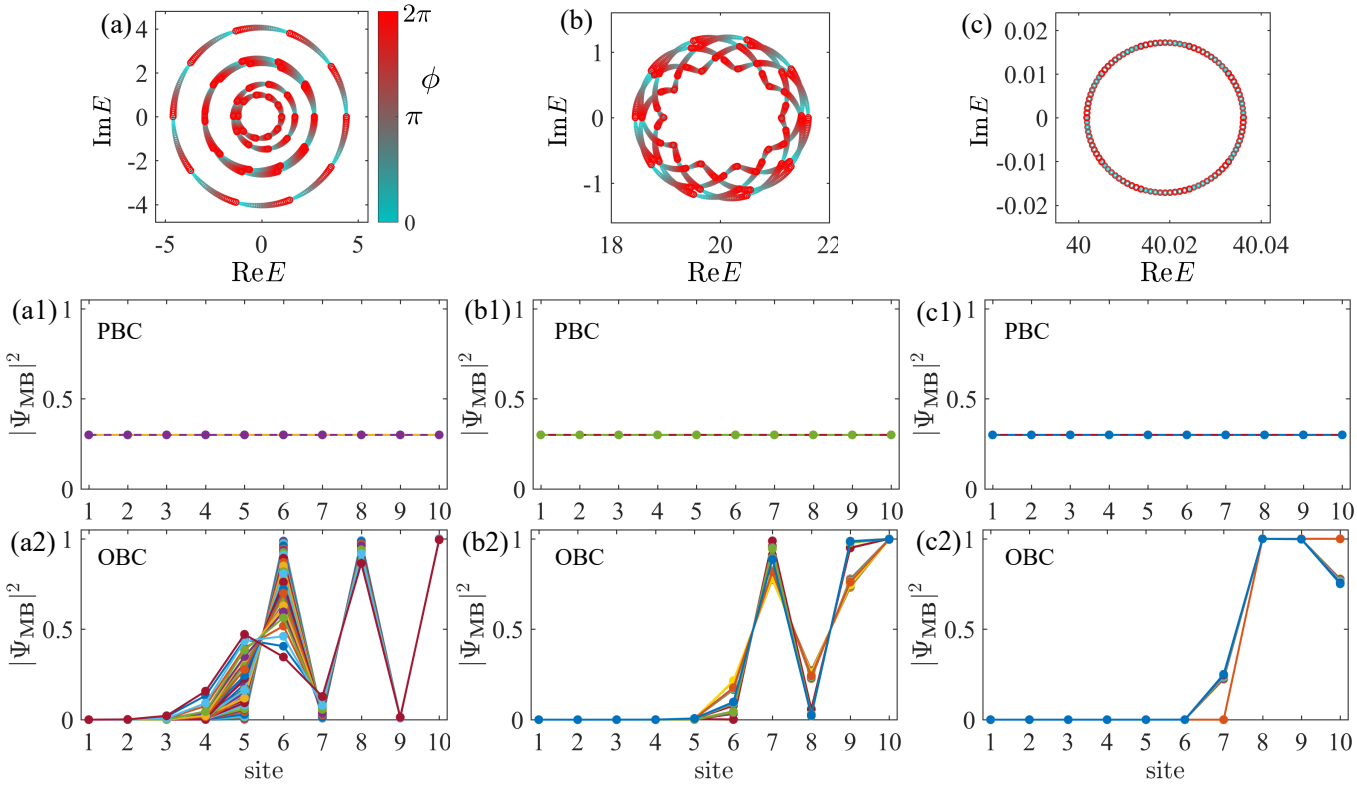

Fig. S5. (a-c) Movement of the eigenenergies of the clusters at $\varepsilon_s = 0$, U and $2U$, respectively, when the twist boundary angle ϕ increases from 0 (cyan) to 2π (red). All eigenenergies belonging to the same cluster wind around the center in one direction. The spectral winding numbers for the three clusters are found as $\nu_s = 5$, 4 and 3, respectively. (a1-c1) Charge density profiles of the eigenstates with energies around $\varepsilon_s = 0$, U and $2U$, respectively, when PBC are imposed. (a2-c2) the same as (a1-c1) but for OBC. The charge-density profiles are markedly different for PBC and OBC. Moreover, the charge densities tend to localize at one open boundary when OBC are imposed. Other parameters are the same as Fig. S4.

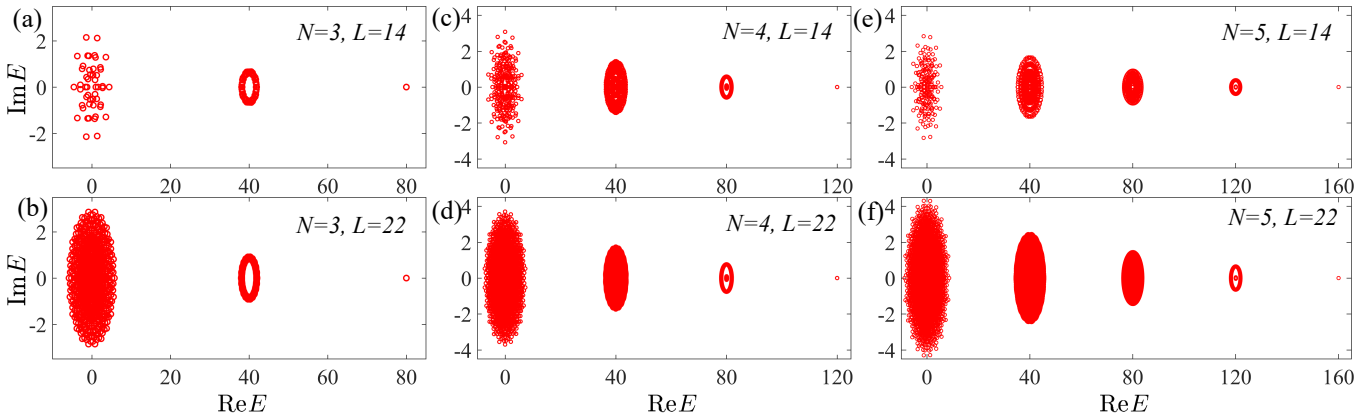

Fig. S6. Spectral clusters for fixed N and increasing L. The right, middle and left panels are for $N = 3$, 4 and 5, respectively. The upper and lower panels are $L = 14$ and 22, respectively. As L grows, the eigenenergies fill the clusters more densely. In the TDL, the clusters occupy continuous areas and orbits around their energy centers in the complex-energy plane.

invariant can be obtained as the winding numbers of these orbits. We note that the extents of the clusters (including the one at $\varepsilon_1 = (N-1)U$) on real and imaginary axes are independent of large L. The extents of the clusters are finite, provided that U is finite.

For single particles, it has been demonstrated that a nonzero spectral winding number inevitably lead to the non-Hermitian skin effect [3, 4]. In the following, we show that this relationship can be generalized to many-body

strongly interacting systems. The point-gap topology with nonzero winding numbers in the PBC spectrum ensures that its difference as compared to the OBC one, thus leading to the non-Hermitian skin effect even in the many-body interacting systems.

We focus on the strong interaction ($U \gg t$) regime where the PBC spectrum develops multiple clusters which are centered at $\varepsilon_s \in \{0, U, ..., (N-1)U\}$ and have nonzero winding numbers, as we discussed before. In this strong interaction regime, we consider the kinetic hopping term

$$\hat{V}_h = \sum_{\ell=1}^{L} [(t+\gamma)\hat{c}_\ell^\dagger \hat{c}_{\ell+1} + (t-\gamma)\hat{c}_{\ell+1}^\dagger \hat{c}_\ell] \tag{24}$$

as a perturbation to the unperturbed Hamiltonian which consists of only the interaction term

$$\hat{H}_{\text{int}} = U \sum_{\ell=1}^{L} \hat{n}_\ell \hat{n}_{\ell+1}. \tag{25}$$

Then, up to the N-order perturbations in $\hat{V}_h$, the effective Hamiltonian projected within cluster $s \in \{1, 2, ..., N\}$ may be written as

$$\hat{H}_{\text{eff}}^{(s)} = (N-s)U + \hat{P}_s \sum_{j=1}^{N} \hat{V}_h [(E - \hat{H}_{\text{int}})^{-1} \hat{V}_h]^{j-1} \hat{P}_s + \mathcal{O}(\hat{V}_h^{N+1}), \tag{26}$$

where $\hat{P}_s$ is the orthogonal projection operator onto the many-body Fock subspace associated with cluster s. Using the perturbation theory, we can derive effective Hamiltonians under PBC and OBC, respectively, for each cluster. From these Hamiltonians, we can find again that the PBC spectrum has a nonzero nonzero winding number whereas the OBC spectrum is always real, which is consistent with our numerical calculations. Indeed, the effective Hamiltonian under OBC can be converted into a Hermitian one via a similarity transformation. Such a similarity transformation does not change the spectrum, and clearly shows the concentration of the many-body eigenstates to the Fock basis state with its particles accumulated close to an open boundary. Therefore, the many-body eigen wavefunctions are localized to the boundary, thus exhibiting the many-body non-Hermitian skin effect.

As an illustration, we consider the cluster $s = 1$. For this cluster, we denote and order the orthogonal many-body basis with the position as

$$|\overline{\ell}\rangle = \hat{c}_\ell^\dagger \hat{c}_{\ell+1}^\dagger ... \hat{c}_{\ell+N-1}^\dagger |\text{vac}\rangle, \quad \ell \in \{1, ..., L\}, \tag{27}$$

where $|\text{vac}\rangle$ is the vaccum state. The effective Hamiltonian under PBC can be derived as

$$\langle \overline{\jmath} | \hat{H}_{\text{eff}}^{(1)} | \overline{\ell} \rangle = \tilde{E}_1 \delta_{\jmath,\ell} + \frac{(t-\gamma)^N}{U^{N-1}} \delta_{\jmath,\ell+1} + \frac{(t+\gamma)^N}{U^{N-1}} \delta_{\jmath,\ell-1}, \tag{28}$$

where $\tilde{\varepsilon}_1 = (N-1)U + E_{1,c}$. Thus, the effective Hamiltonian is given by

$$\hat{H}_{\text{PBC}}^{(1)} = \tilde{\varepsilon}_1 + \sum_{\ell=1}^{L} \Big[\frac{(t-\gamma)^N}{U^{N-1}} |\overline{\ell+1}\rangle\langle\overline{\ell}| + \frac{(t+\gamma)^N}{U^{N-1}} |\overline{\ell}\rangle\langle\overline{\ell+1}| \Big]. \tag{29}$$

This Hamiltonian takes a similar form as the single-particle Hatano-Nelson model but is defined on the basis of Fock states. In the $N = 1$ limit, it recovers the single-particle Hamiltonian. The E_{shift} in Eq. (29) stems from the even-order corrections. It shifts the energy of the cluster globally in real axis and thus does not affect the topology of the system of interest. To the second-order corrections, the energy shift can be estimated as $E_{1,c} \approx 2(t^2 - \gamma^2)/U$. The hopping terms are dominated by the N-order correction. They are non-reciprocal in the orthogonal Fock subspace: the hopping amplitude from the many-body state $|\overline{\ell}\rangle$ to the next one $|\overline{\ell+1}\rangle$ is $(t-\gamma)^N/U^{N-1}$, while the hopping amplitude for the inverse process is instead $(t+\gamma)^N/U^{N-1}$. By Fourier transformation, the energy spectrum can be found as

$$\widetilde{E}_{\text{PBC}}^{(1)} = \tilde{\varepsilon}_1 + \frac{(t-\gamma)^N}{U^{N-1}} e^{-iq} + \frac{(t+\gamma)^N}{U^{N-1}} e^{iq}, \tag{30}$$

where $q \in \{0, 2\pi/L, 4\pi/L, ..., 2\pi\}$ can be viewed as the momentum of the many-body eigenstates. This spectrum is consistent with the numerical calculations, as shown in Fig. S7. From Eq. (30), we also see that in the TDL ($L \to \infty$),

the spectrum forms a closed loop in the complex-energy plane, similar to that of the single-particle Hatano-Nelson model [cf. Fig. S7(b)]. Taking into account the magnetic flux, the spectrum becomes

$$\widetilde{E}^{(1)}_{\rm PBC}(\phi)=\tilde{\varepsilon}_1+e^{-iN\phi/L}e^{-iq}+e^{iN\phi/L}e^{iq}\frac{(t+\gamma)^N}{U^{N-1}}. \tag{31}$$

Using Eq. (3) in the main text, we obtain the winding number as $\nu_1=\mathrm{sgn}(\gamma)N$, which again is consistent with our numerical calculations [c.f. Fig. S7(c)].

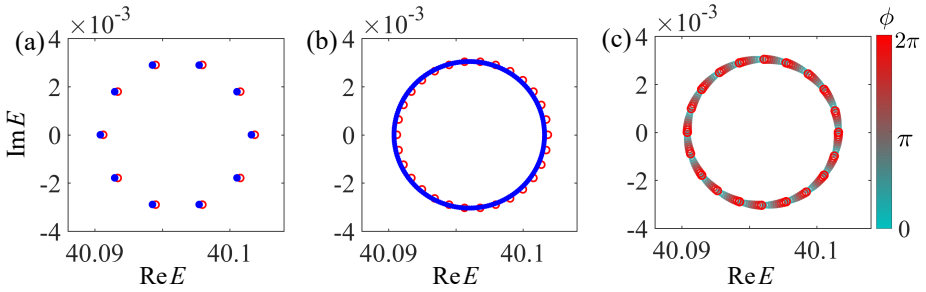

Fig. S7. (a) Many-body spectrum (blue) obtained by the effective model in Eq. (29). The red circles are obtained by exact diagonalizing the full many-body Hamiltonian and are plotted for comparison. (c) Many-body spectrum (blue) obtained by the effective model in Eq. (30) in the TDL. The red circles are obtained by exact diagonalizing the full many-body Hamiltonian with $L=30$ sites and are plotted for comparison. (c) Evolution of many-body spectrum (blue) obtained by the effective model in Eq. (31) by increasing the twist angle ϕ from 0 to 2π. We consider $N=3$, $\gamma=0.2t$, $U=20t$, $t=1$, $s=1$ and PBC in all panels, and $\phi=0$ in (a) and (b).

Next, we impose OBC (i.e., termination of the coupling between the $\ell=1$ and L sites) and derive the effective Hamiltonian as

$$\hat{H}^{(1)}_{\rm OBC}=\tilde{\varepsilon}_1-\sum_{\ell=1}^{N-1}E_\ell(|\overline{\ell}\rangle\langle\overline{\ell}|+|\overline{L-\ell}\rangle\langle\overline{L-\ell}|)+\sum_{\ell=1}^{L-N}\frac{(t-\gamma)^N}{U^{N-1}}|\overline{\ell+1}\rangle\langle\overline{\ell}|+\frac{(t+\gamma)^N}{U^{N-1}}|\overline{\ell}\rangle\langle\overline{\ell+1}|. \tag{32}$$

Note that under OBC, we have $L-N+1$ many-body states in cluster $s=N$. Due to the termination, the Fock basis states close to the two ends have different potential corrections compared to those deep in the bulk. Following the spirit of Refs. [3, 4], one can show that the Hamiltonian with open boundaries is always topological trivial in terms of point gaps. To be explicit, we can apply a similarity transformation

$$|\overline{\ell}\rangle\to\eta^\ell|\overline{\ell}\rangle,\quad \langle\overline{\ell}|\to\eta^{-\ell}\langle\overline{\ell}|,\qquad (\ell\in\{1,...,L-N+1\}), \tag{33}$$

where $\eta=|(t+\gamma)/(t-\gamma)|^{N/2}$, and transfer the Hamiltonian (32) to a Hermitian one

$$\hat{H}^{(1)\prime}_{\rm OBC}=\tilde{\varepsilon}_1-\sum_{\ell=1}^{N-1}E_\ell(|\overline{\ell}\rangle\langle\overline{\ell}|+|\overline{L-\ell}\rangle\langle\overline{L-\ell}|)+\frac{(t^2-\gamma^2)^{N/2}}{U^{N-1}}\sum_{\ell=1}^{L-N}(|\overline{\ell+1}\rangle\langle\overline{\ell}|+|\overline{\ell}\rangle\langle\overline{\ell+1}|). \tag{34}$$

The similarity transformation does not change the spectrum. Thus, the effective Hamiltonian (32) under OBC has a purely real spectrum, topologically different from that under PBC. In the TDL, we approximate the spectrum as

$$\widetilde{E}^{(1)}_{\rm OBC}\approx\tilde{\varepsilon}_1+2\frac{(t^2-\gamma^2)^{N/2}}{U^{N-1}}\cos q, \tag{35}$$

where $q\in\{0,2\pi/(L-N+1),4\pi/(L-N+1),...,2\pi\}$. The OBC spectrum forms a line in real axis inside the PBC spectrum (i.e., closed loop) (see Fig. S8). This result indicates that most and extensive many-body eigenstates under OBC are localized to one open boundary. These results are also consistent with our numerical calculations.

In fact, from the similarity transformation, we can further see that for $N\ll L$, the many-body eigenstates tend to concentrate to the Fock basis state $|\overline{L-N+1}\rangle$ if $|\eta|>1$ while to the state $|\overline{1}\rangle$ if $\eta<1$. Note that the wavefunction of the basis state $|\overline{\ell}\rangle$ are accumulated from sites ℓ to $\ell+N-1$. Thus, the many-body eigen wavefunctions are localized at the right end if $\eta>1$ while at the left end if $\eta<1$. When $\gamma=0$, the spectral winding numbers become ill-defined. Accordingly, the similarity transformation become trivial with $\eta=1$, and thus the many-body skin effect

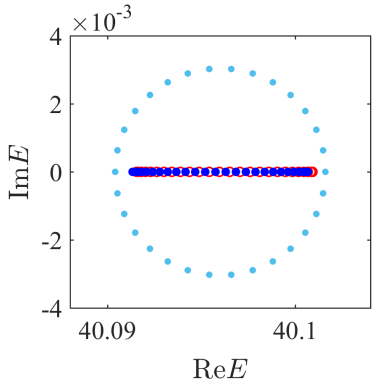

Fig. S8. (a) Many-body spectrum (blue dots) obtained by the effective model in Eq. (32). The red circles are obtained by exact diagonalizing the full many-body Hamiltonian. The cyan dots are the spectrum under OBC. Other parameters are the same as those in Fig. S7.

disappears. From this aspect, we see clearly that the nontrivial spectral winding number and the many-body skin effect are intimately related.

The above derivation can be generalized to other clusters, which is relatively more complicate. However, the essential results are the same: the many-body system can be understood as a "single-particle" model defined on the basis of Fock states, and the OBC effectively terminate the direct coupling between the "boundary" Fock basis states whose particles accumulated towards the boundaries. The nontrivial spectral topology of the PBC spectrum leads to the localization of the many-body eigenstates to the boundary Fock states, in the same manner as that in single-particle system, which hence exhibit the localization of the many-body eigen wavefunctions towards the boundaries. Finally, it may be also worth noting that for other clusters, the non-reciprocal hopping between the Fock basis states can be obtained by lower-order corrections. Thus, we find stronger effective nonreciprocity and hence larger spectral areas for these clusters. This is also confirmed by our numerical observations [Fig. 4(b) in the main text].

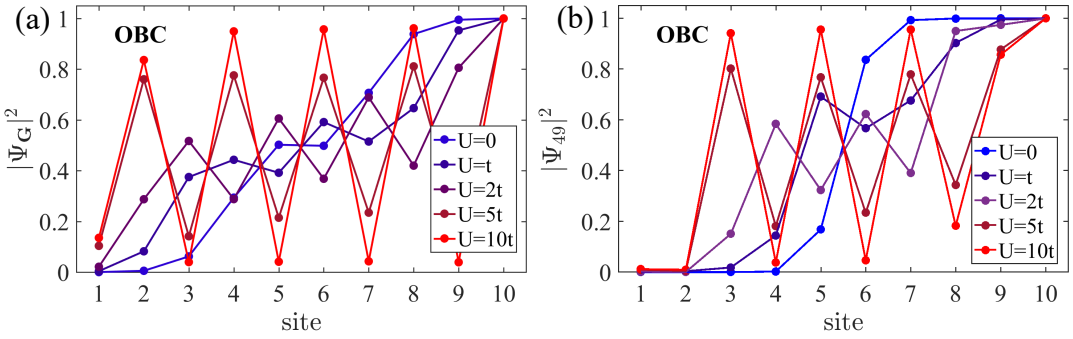

Fig. S9. Charge-density profiles of many-body states for $U = 0$, t, $2t$, $5t$ and $10t$, respectively. Two states, namely, (a) the ground state and (b) the 50th lowest-Re(E) states, are taken for illustrations. With increasing U, the charge-density profile of the many-body states become extended over the whole lattice chain with open boundaries. $L = 10$, $N = 5$ and other parameters are the same as Fig. S5

In contrast, at half-filling and for $|\gamma| < t$ ($|\gamma| > t$), the many-body spectrum of a finite system under PBC shrinks onto the real axis (open lines parallel to the imaginary axis) as U increase. Accordingly, we observe that upon increasing U, the charge-density profile of the many-body states become extended over the whole lattice chain with open boundaries, as shown in Fig. S9. For concreteness and brevity, we show the results for two states in Fig. S9. We note that all other many-body states exhibit similar behaviors.

VIII. OTHER HALF-FILLED CASES

In the main text, we have discussed (I) the half-filled cases with odd (even) $N = L/2$ and (anti-)PBC. In this section, we discuss the results for the complementary half-filled cases (II), namely, with even (odd) N and (anti-)PBC. In the cases (II), the system has always two ground states with complex-conjugate energies; and there is no exceptional point between two lowest excited states, as shown in Figs. S10(a) and (b). Thus, we do not observe the two $\mathcal{PT}$ transitions. However, we observe that as the size of the system L grows, the excitation gap $\Delta_{\rm gap}$ becomes vanishingly small for $U < U_c'$ and increases rapidly for $U > U_c'$, and the critical interaction strength U_c' approaches with that one (U_c) characterizing the low-energy $\mathcal{TP}$ transition in the cases (I) [cf. Fig. S10(c)]. This result indicates that in the TDL, the phase transition from the gapless regime to the gapped CDW regime happens also in the cases (II) and the corresponding critical interaction strength coincides with that in the cases (I).

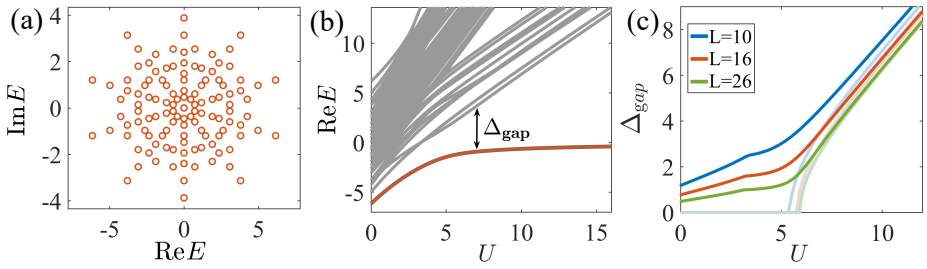

Fig. S10. Results for the cases with even (odd) $N = L/2$ and (anti-)PBC. (a) Many-body spectrum at half-filling in the absence of interactions ($U = 0$). (b) Real part of the low-energy many-body spectrum as a function of U. We take $L = 10$ for illustration. (c) Excitation gap $\Delta_{\rm gap}$ as a function of U. The light colored lines are the results for cases (I) and presented here for comparison. We see that as $L \to \infty$, the metal-insulator transition in cases (II) resemble that in cases (I). Other parameters are the same as that in Fig. 3 in the main text, namely $L = 10$ in panels (a) and (b), and $\gamma = 0.6t$ in all panels.

IX. CALCULATIONS FOR THE NON-HERMITIAN SSH-TYPE MODEL

Our main results, such as the symmetry-breaking phase transitions and nontrivial spectral topology, revealed from the interacting Hatano-Nelson model are general. They can also be applied to other models. As an example, we consider the Su-Schrieffer-Heeger (SSH) type model in which non-reciprocal hopping occurs every two nearest-neighbour bonds, as sketched in Fig. S11(a). The non-Hermitian SSH-type Hamiltonian reads

$$H = \sum_{\ell} \Big\{ (\hat{C}_\ell^\dagger (t\sigma_x - i\gamma\sigma_y)\hat{C}_\ell + \frac{t}{2}[\hat{C}_{\ell+1}^\dagger(\sigma_x + i\sigma_y)\hat{C}_\ell + h.c.] \Big\}, \tag{36}$$

where $\hat{C}_\ell \equiv (\hat{c}_{A,\ell}, \hat{c}_{B,\ell})^T = (\hat{c}_{2\ell-1}, \hat{c}_{2\ell})^T$ with A and B indicating odd and even lattice sites, respectively. The Pauli matrices act on sublattice space consisting of A and B. $h.c.$ indicates Hermitian conjugation of the previous term. Figure S11(c) illustrates the flow of the full spectrum of the model with size $L = 12$ and half-filling under anti-PBC. We see clearly that both the low-energy and full $\mathcal{PT}$ phase transitions occurs in the non-Hermitian SSH-type model as we increase the strength of nearest neighbor interaction. We have also checked that as L increases, while the critical strength $U_{c,all}$ for the full $\mathcal{PT}$ transition increases monotonically, the critical strength U_c for the low-energy $\mathcal{PT}$ transition saturates to a finite value. The non-Hermitian SSH-type model also exhibits the nontrivial winding in the spectrum, as shown in Fig. S12. All these features are the same as those in the interacting Hatano-Nelson model (up to that the imaginary energies are half of those of the Hatano-Nelson model).

It may be worthy noting that through a local unitary transformation $\hat{C}_\ell \to 1/\sqrt{2}(\sigma_0 + i\sigma_x)\hat{C}_\ell$, the model (36) can be converted to a Creutz-ladder-like model [5]

$$H = \sum_{\ell} \Big\{ (\hat{C}_\ell^\dagger (t\sigma_x + i\gamma\sigma_z)\hat{C}_\ell + \frac{t}{2}[\hat{C}_{\ell+1}^\dagger(\sigma_x - i\sigma_z)\hat{C}_\ell + h.c.] \Big\}. \tag{37}$$

Notably, the non-Hermiticity in the Creutz-ladder-like model contains pure onsite gain ($i\gamma$) and loss ($-i\gamma$) [see Fig. S11(a)]. The interaction term can be transformed accordingly and remains Hermitian after the transformation.

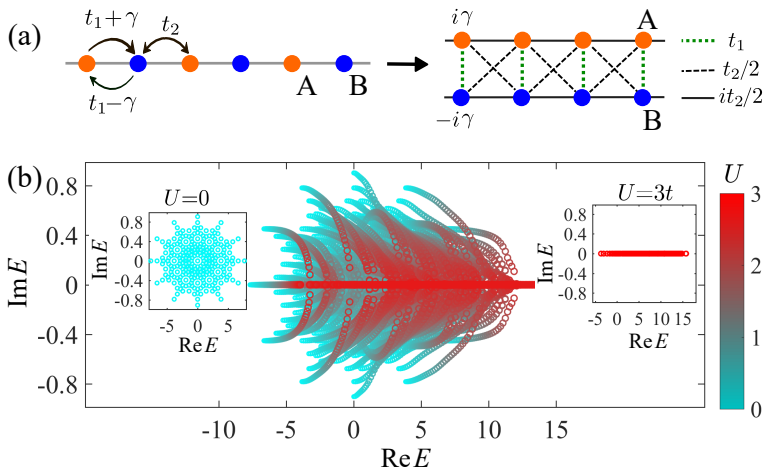

Fig. S11. (a) Schematic for the non-Hermitian SSH-type model (left panel). The orange and blue dots indicate two sublattices (A and B), respectively. The nonreciprocal hopping occurs only within unit cells. The model can be converted to a Creutz-ladder-like model with imaginary hopping and onsite gain and loss (right panel). (b) $\mathcal{PT}$ transitions in the interacting non-Hermitian SSH-type lattice chain with $L = 12$, $N = 6$ and $\gamma = 0.2t$. The changing colour (from cyan to red) indicates the change of interaction strength from $U = 0$ to $3t$. The insets show the spectra at $U = 0$ and $3t$, respectively. We consider anti-PBC for illustration.

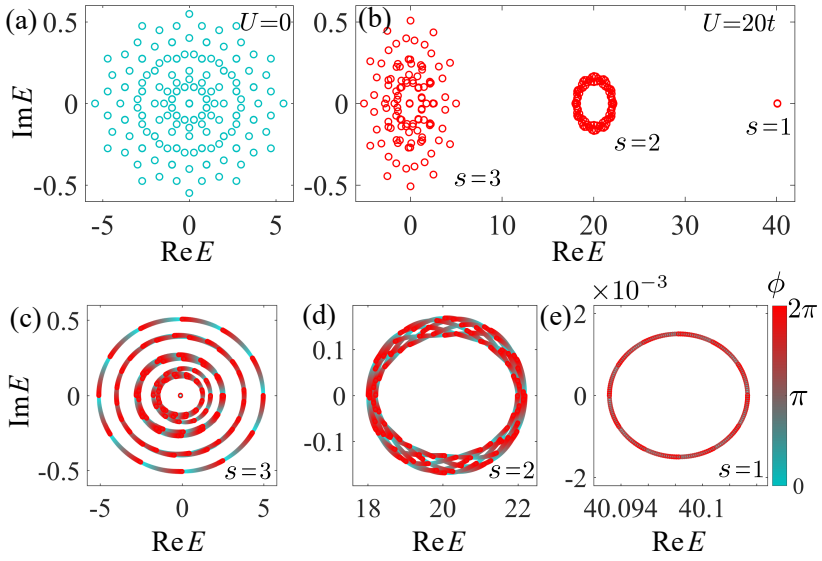

Fig. S12. Energy spectrum of the interacting SSH-type lattice chain with $L = 12$, $N = 3$ and $\gamma = 0.2t$. (a) and (b) are the spectra at $U = 0$ and $20t$ respectively. (c), (d) and (e) display respectively the movement of the three spectral clusters (labeled by $s = 1, 2, 3$) as varies ϕ from 0 (cyan) to 2π (red).

The dissipative Hamiltonian (37) can be directly derived from the Lindblad equation as we show in the following. The Lindblad equation under the Markov approximation reads [6]

$$\frac{d\rho}{dt} = -i[H_0, \rho] + \sum_{\ell} \Big(L_\ell \rho L_\ell^\dagger - \frac{1}{2}\{L_\ell^\dagger L_\ell, \rho\} \Big), \tag{38}$$

where $\rho(t)$ is the density matrix of the system at time t. H_0 is the system Hamiltonian in the absence of coupling to environment. It is Hermitian and prepared as

$$H_0 = \sum_{\ell} t \Big\{ \hat{C}_\ell^\dagger \sigma_x \hat{C}_\ell + \frac{1}{2}[\hat{C}_{\ell+1}^\dagger (\sigma_x - i\sigma_z)\hat{C}_\ell + h.c.] \Big\}. \tag{39}$$

L_ℓ are the Lindblad jump operators in terms of fermion operators. We consider one-body loss events described by

$L_\ell = g_\ell \hat{c}_\ell$ with $g_\ell = i^\ell \sqrt{2\gamma}$. The coefficients g_ℓ are determined from the loss rates of atoms. Following the quantum trajectory method [7], the dynamics of the system can be decomposed into a Schrödinger evolution under an effective non-Hermitian Hamiltonian and quantum-jump processes which induce particle losses with the jump operators L_ℓ,

$$\frac{d\rho}{dt} = -i(H_{\text{eff}}\rho - \rho H_{\text{eff}}^\dagger) + \sum_\ell L_\ell \rho L_\ell. \tag{40}$$

We find that the resulting effective Hamiltonian

$$H_{\text{eff}} = H_0 - \frac{i}{2}\sum_\ell L_\ell^\dagger L_\ell = H_0 + i\gamma \sum_\ell \hat{C}_\ell^\dagger \sigma_z \hat{C}_\ell \tag{41}$$

gives exactly the dissipative Creutz model in Eq. (37). It describes the evolution of the system during a time interval between quantum jump events. If we consider a situation where the equilibration time in the measured many-body system is shorter than a typical time between quantum jumps, it is justified to consider only H_{eff} for the short-time evolution.

[1] M. H. Kalthoff, D. M. Kennes, and M. A. Sentef, "Floquet-engineered light-cone spreading of correlations in a driven quantum chain", Phys. Rev. B **100**, 165125 (2019).

[2] N. Byers and C. N. Yang, "Theoretical considerations concerning quantized magnetic flux in superconducting cylinders", Phys. Rev. Lett. **7**, 46 (1961).

[3] K. Zhang, Z. Yang, and C. Fang, "Correspondence between Winding Numbers and Skin Modes in Non-Hermitian Systems", Phys. Rev. Lett. **125**, 126402 (2020).

[4] N. Okuma, K. Kawabata, K. Shiozaki, and M. Sato, "Topological origin of non-hermitian skin effects", Phys. Rev. Lett. **124**, 086801 (2020).

[5] E. J. Bergholtz, J. C. Budich, and F. K. Kunst, "Exceptional topology of non-Hermitian systems", Rev. Mod. Phys. **93**, 015005 (2021).

[6] G. Lindblad, "On the generators of quantum dynamical semigroups", Commun. Math. Phys. **48**, 119 (1976).

[7] A. J. Daley, "Quantum trajectories and open many-body quantum systems", Adv. Phys. **63**, 77 (2014).